UC Irvine
UC Irvine Previously Published Works

Title

Energy flow between spectral components in 2D broadband stimulated Raman spectroscopy

Permalink

https://escholarship.org/uc/item/0j61v54j

Journal

Physical Chemistry Chemical Physics, 17(16)

ISSN

0956-5000

Authors

Batignani, G
Fumero, G
Mukamel, S
et al.

Publication Date

2015-04-28

DOI

10.1039/c4cp05361c

Copyright Information

Peer reviewed

PCCP

CrossMark
click for updates

Energy flow between spectral components in 2D broadband stimulated Raman spectroscopy†

G. Batignani,[ab] G. Fumero,[a] S. Mukamel[c] and T. Scopigno*[ad]

We introduce a general theoretical description of non resonant impulsive femtosecond stimulated Raman spectroscopy in a multimode harmonic model. In this technique an ultrashort actinic pulse creates coherences of low frequency modes and is followed by a paired narrowband Raman pulse and a broadband probe pulse. Using closed-time-path-loop (CTPL) diagrams, the response on both the red and the blue sides of the broadband pulse with respect to the narrowband Raman pulse is calculated, the process couples high and low frequency modes, which share the same ground state. The transmitted intensity oscillates between the red and the blue side, while the total number of photons is conserved. The total energy of the probe signal is periodically modulated in time by the coherence created in the low frequency modes.

1 Introduction

Nonlinear optical techniques have been widely employed in time resolved studies of vibrational dynamics of complex molecular and solid state systems.

Stimulated Raman Scattering (SRS) is a nonlinear third order four-wave mixing process, which is coherently driven when the energy difference between two laser pulses is resonant with a Raman active molecular transition. Scattering from the interacting medium generates blue and red shifted components with an efficiency which is enhanced by many orders of magnitude relative to spontaneous Raman scattering signals.

Femtosecond stimulated Raman spectroscopy (FSRS) is a fifth order pump probe technique recently introduced,[1,2] which uses SRS as a probe.[3–13] It has been shown to provide an improved spectral and temporal resolution compared to time-resolved spontaneous Raman spectroscopy. In a typical FSRS experiment, a femtosecond electronically resonant actinic pump pulse triggers vibrational dynamics in an electronically excited state; then, after a variable time delay, the joint action of a picosecond Raman pulse and a femtosecond broadband continuum pulse generates a vibrational coherence, which allows us to probe the state of the system *via* the SRS process.

The detected signal given by the frequency dispersed transmission of the broadband probe shows both the gain and loss of Raman features at the red and blue side of the narrowband Raman pulse spectrum.[14,15]

In this paper, we address a different scenario in which a femtosecond electronically off-resonant actinic pulse ε_a acts impulsively on the sample to generate a ground state coherence rather than an excited state coherence. Depending on the bandwidth of the actinic pulse ($\Delta T_A \simeq 50$ fs, which corresponds to 300 cm^{-1} for a transform limited Gaussian envelope of routinely available ultrafast laser sources), only relatively low frequency modes (≤ 300 cm^{-1}) of the sample can be excited, leaving it in a vibrationally coherent superposition state. Under such circumstances, an ultrashort pulse passing through a medium experiences an upward or downward frequency shift depending on its relative timing after the actinic pulse,[16] *i.e.* a third order Raman process with oscillating Stokes and anti-Stokes intensities is generated. The classical, macroscopic view of this effect is that the molecular vibration, induced by the actinic pulse, generates temporal oscillations in the refractive index. The associated time dependent phase induces a blue or a red frequency shift, depending on the derivative sign. These low frequency modes can also couple,[17,18] even in the harmonic limit,[19] to time delayed Stimulated Raman probing of higher frequency modes, generating a fifth order polarization. It has been already emphasized[18,20] that in molecular liquids the fifth order polarization signals are orders of magnitude smaller than the third order ones and need an attenuation of the overwhelming cascade processes to be detectable. On the other hand, fifth order and cascading processes can be distinguished by their different dependence on chromophore density (linear for the former and quadratic for the latter). Therefore cascading can be suppressed by working

[a] *Dipartimento di Fisica, Universitá di Roma "Sapienza", I-00185 Roma, Italy*
[b] *Dipartimento di Scienze Fisiche e Chimiche, Universitá degli Studi dell'Aquila, I-67100, L'Aquila, Italy*
[c] *Department of Chemistry, University of California, Irvine, California 92697-2025, USA*
[d] *Centre for Life Nano Science – IIT@Sapienza, Istituto Italiano di Tecnologia, I-00161 Roma, Italy*

at lower densities, which becomes feasible as detection sensitivity is improved. In general, that fifth order processes can be measured in molecular liquids has been demonstrated by R. J. Miller[21,22]. Here we extend previous studies of the fifth order polarization within a completely new framework, elucidating the precise microscopic mechanism for the energy transfer between different spectral components of the dispersed FSRS response. The actinic pulse initiates the low frequency vibrational coherences at time $t = 0$, then, after a time delay T, the Raman pulse ε_p and the broadband continuum pulse ε_s stimulate the Raman scattering of a higher frequency vibrational mode. The resulting 2D signal $S(\omega,T)$ depends on the dispersed probe frequency ω and the delay T. Photoinduced structural changes (not included here for the sake of simplicity) could cause additional frequency variations. The response of the system is derived by using closed-time-path-loop (CTPL) diagrams; both the red and the blue sides of the spectrum are calculated, providing a unified description of gain and loss processes. Analysis of the two regimes shows that the number of photons of the ε_s field oscillates with T with the opposite phase and the same amplitude in the red and in the blue side, therefore the total number of photons is conserved during the process; the total energy of the ε_s field, obtained by the first moment of the transmitted probe frequency profile, shows a damped oscillation. This analysis allows us to rationalize third-order experiments such as those reported in ref. 16 and 23.

2 Expressions for FSRS signals

The FSRS process is described by the Hamiltonian

$$H = H_0 + H' + H_f$$

where H_0, H_f and H' represent the free molecule, the radiation field and the effective radiation–matter interaction, respectively. For electronically off-resonance pulses, an excitation to a virtual state is accompanied by an instantaneous de-excitation to a real state, since by the Heisenberg uncertainty principle the system can only spend a very short time on the intermediate state. Therefore, in the rotating wave approximation (RWA), H' reads:

$$H'(t) = \alpha(t) \sum_{i,j} \varepsilon_j^\dagger(t)\varepsilon_i(t) + \text{h.c.} \tag{1}$$

where α is the excited state polarizability

$$\alpha = \sum_{a \neq b} \alpha_{ab} |a\rangle\langle b|$$

and $\varepsilon = \sum_j \varepsilon_j$ and $\varepsilon^\dagger = \sum_j \varepsilon_j^\dagger$ are the positive and the negative frequency components of the total electric field operator:

$$E(\mathbf{r}, t) = \sum_j \varepsilon_j(t)e^{i\mathbf{k_j}\cdot\mathbf{r}} + \sum_j \varepsilon_j^\dagger(t)e^{-i\mathbf{k_j}\cdot\mathbf{r}} \tag{2}$$

For non-overlapping $\varepsilon_a(t)$ and $\varepsilon_s(t)$ pulses, eqn (1) reduces to

$$H'(t) = \alpha(t)\left[\varepsilon_s^\dagger(t)\varepsilon_p(t) + \varepsilon_a^\dagger(t)\varepsilon_a(t)\right] + \text{h.c.} \tag{3}$$

Where ε_a is not coupled to the other fields. This corresponds to the pump–probe technique where the actinic pump generates a photo-excitation that is then detected by the probe. This picture

holds also for an off-resonant actinic pulse that generates a ground state coherence.

Stimulated optical signals can be defined as the time derivative of the mean number of photons[24]

$$
\begin{aligned}
S &= \int_{-\infty}^{+\infty} dt \frac{d}{dt}\left\langle a_i^\dagger(t)a_i(t)\right\rangle = \frac{2}{\hbar}\Im\int_{-\infty}^{+\infty} dt' \left\langle P(t')\varepsilon^\dagger(t')\right\rangle \\
&= \frac{2}{\hbar}\Im\int_{-\infty}^{\infty} \frac{d\omega'}{2\pi}\Im\left\langle P(\omega')\varepsilon^\dagger(\omega')\right\rangle
\end{aligned}
\tag{4}
$$

where

$$P(\omega) = \int_{-\infty}^{+\infty} dt\, e^{i\omega t} P(t) \tag{5}$$

and $P(t) = Tr[V\rho(t)]$ is the nonlinear polarization induced by the interaction and $\langle \ldots \rangle = Tr[\rho(t)\cdot\ldots]$. The frequency-gated signal is then given by

$$S(\omega, T) = \frac{2}{\hbar}\Im\varepsilon_s^*(\omega)\int_{-\infty}^{+\infty} e^{i\omega t}\left\langle TP(t)e^{-\frac{i}{\hbar}\int_{-\infty}^{+\infty} dt' H'_-(t')}\right\rangle \tag{6}$$

where H'_- is the Liouville superoperator in the interaction picture and T indicates the superoperator time ordering. This expression can be expanded perturbatively in field–matter interactions. In the present application we expand the exponential to fifth order in the fields which yields the 5th order polarization $P^{(5)}$.

The 5th order off-resonant polarization is a convolution of the fields with a three point correlation function of the susceptibility operator. Using the loop diagram representation, it can be easily written directly from the diagram by the application of the rules given in ref. 25. The diagrams that contribute to the broadband FSRS process are given in Fig. 1. Usually the expressions for the detected signals are derived in terms of nonlinear susceptibilities, using a semiclassical approach, where classical fields interact with a quantum system and they can easily be represented by double sided Feynman diagrams or energy level diagrams. While the conventional double sided Feynman diagram description is based on the density matrix (Liouville N^2 dimensional space), the CTPL diagram description, used in this work, is based on the wavefunction (Hilbert N dimensional space). In the CTPL description the ket (bra) evolution is described by a forward (backward) propagation of the wave function; in the CTPL there is no time-ordering between the left hand side (ket) of the diagram and the right hand side (bra), resulting in fewer contributing terms for a given signal.

We shall work in the frequency domain using a Fourier transform of the field envelopes and define the retarded Green's function

$$G(\omega) = \frac{1}{\hbar(\omega - H_0 + i\eta)} = \frac{1}{\hbar}\sum_\nu \frac{|\nu\rangle\langle\nu|}{\omega - \omega_\nu + i\gamma} \tag{7}$$

and the advanced Green's function

$$G^\dagger(\omega) = \frac{1}{\hbar(\omega - H_0 - i\eta)} = \frac{1}{\hbar}\sum_\nu \frac{|\nu\rangle\langle\nu|}{\omega - \omega_\nu - i\gamma} \tag{8}$$

In both eqn (7) and (8) η is a positive infinitesimal that ensures causality and further guarantees the convergence of
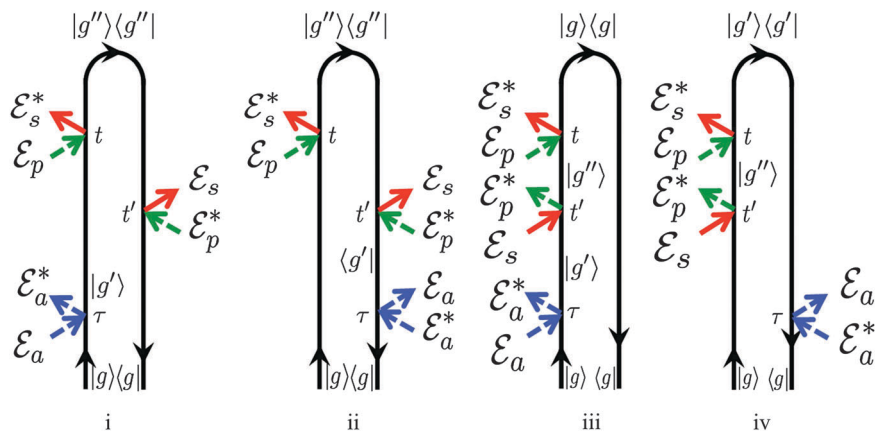
Fig. 1 Closed-time-path-loop diagrams for stimulated Raman with an impulsive actinic pump preceding the ε_s field, under off-resonance conditions. g refers to the ground state while g' and g'' range over all the vibrational frequencies.

the Fourier transform. The right hand side of the equations is obtained by an expansion in the molecular eigenstate basis $|\nu\rangle$ and γ is the vibrational dephasing rate.

By reading off the diagrams, we obtain:

$$S(\omega, T) = (-1)^3 P_g \Im \int_{-\infty}^{+\infty} \frac{d\Delta_P}{2\pi} \frac{d\omega'_P}{2\pi} \frac{d\Delta}{2\pi} \frac{d\Delta_A}{2\pi} \frac{d\omega'_A}{2\pi}$$
$$\times 2\pi\delta(\Delta_P - \Delta_A - \Delta)e^{-i\Delta_A T}$$
$$\times \varepsilon_P(\omega'_P)\varepsilon_P^*(\omega'_P + \Delta_P)\varepsilon_s(\omega + \Delta)\varepsilon_S^*(\omega)\varepsilon_a(\omega'_A + \Delta_A)$$
$$\times \varepsilon_A^*(\omega'_A)(F_i + F_{ii} + F_{iii} + F_{iv}) \tag{9}$$

where $P_i = \left[1 + e^{\beta(E_i - E_g)}\right]^{-1}$, with $\beta = 1/(k_B T)$, represents the thermal occupation of state i and all the relevant information about the matter is contained in the following correlation functions of the molecular polarizability which correspond to diagrams (i)–(iv).

$$F_i = \langle \alpha G^\dagger(\omega'_P - \omega + \Delta_A)\alpha G(\Delta_A)\alpha \rangle \tag{10}$$

$$F_{ii} = \langle \alpha G^\dagger(\omega'_P - \omega)\alpha G^\dagger(\Delta - \Delta_P)\alpha \rangle \tag{11}$$

$$F_{iii} = \langle \alpha G(\Delta_A)\alpha G(\omega + \Delta - \omega'_P - \Delta_P + \Delta_A)\alpha \rangle \tag{12}$$

$$F_{iv} = \langle \alpha G^\dagger(\Delta - \Delta_P)\alpha G(\omega + \Delta - \omega'_P - \Delta_P)\alpha \rangle \tag{13}$$

The delta function in eqn (9) represents the conservation of field energy. The ground state was excluded in eqn (7) and (8) because that would give a DC background; we are interested in isolating the contributions to the signal due to the excitation of the low frequency modes. The dominant contribution to the signal $S(\omega, T)$ originates from the spectral region in which the denominators of the relevant Green's functions (7) and (8) vanish. The correlation functions (10) and (11) contain an advanced Green's function whose argument contains $\omega'_P - \omega$; diagrams (i) and (ii) then give rise to features on the red side of the Raman pulse. Similarly, diagrams (iii) and (iv) lead to signals on the blue side because the retarded Green's function in correlation functions (12) and (13) contains $\omega - \omega'_P$.

The contributions from both sides of the stimulated Raman spectrum have been denoted Stokes and anti-Stokes processes. We next clarify this terminology. The classification of Raman processes as either *Stokes* or *anti-Stokes* originated in spontaneous Raman. The application of this terminology to the stimulated processes has been a source of confusion. According to the common nomenclature, the distinction between Stokes and anti-Stokes processes is based on the temporally last Raman interaction. One speaks of a Stokes process when, due to the last interaction, the molecule passes from a state of lower to higher energy and the emission is red-shifted; conversely in anti-Stokes the last transition is from a state of higher energy to one of lower energy and the emission is blue-shifted. The term coherent anti-Stokes Raman spectroscopy (CARS) comes from this convention. One can alternatively distinguish Stokes and anti-Stokes processes by looking at the overall energy transfer between the matter and field, during the entire process with all interactions, not just the last. Stokes processes start from the ground state, $|g\rangle \rightarrow |l/h\rangle$, while anti-Stokes processes start from vibrational excited states, $|l/h\rangle \rightarrow |g\rangle$. To avoid confusion we simply refer to these signals as red or blue.

The Raman resonance frequencies in a specific diagram depend on the Liouville space pathway. For example, in diagram (ii), the pathway $|g\rangle \rightarrow |g'\rangle \rightarrow |g''\rangle$ (with g' and g'' indicating two different vibrational levels of the sample) leads to a response at $\omega_P - \omega''_g$ while the pathway $|g\rangle \rightarrow |g'\rangle \rightarrow |g'\rangle$ leads to a response at $\omega_P - \omega'_g$. This can be seen from the argument of Green's functions in correlation functions (eqn (11)). Hereafter we discuss explicitly the pathways that include both ω'_g and ω''_g; the derivation for the $|g\rangle \rightarrow |g'\rangle \rightarrow |g'\rangle$ pathway is similar.

Diagram (i) leads to a feature at $\omega_P - \left(\omega''_g - \omega'_g\right)$. Similarly on the blue side of the Raman pulse, diagram (iii) gives rise to a feature at $\omega_P + \omega''_g$ while (iv) gives a response at $\omega_P + \left(\omega''_g - \omega'_g\right)$. Therefore there are pathways in Liouville space that do not depend on a single mode but contribute to the signal when different vibrational modes share the same ground state.

In order to simplify eqn (9), we use the delta function to carry out the integration over Δ, the bandwidth of the broad

ε_s pulse; assuming a monochromatic Raman pulse $\varepsilon_p(\omega) = 2\pi E_p \delta(\omega - \omega_P)$ we can reduce eqn (9), without loss of generality, to two integrations:

$$S(\omega, T) = (-1)^3 |E_p|^2 P_g \Im \left[\varepsilon_S^*(\omega) \int_{-\infty}^{+\infty} \frac{d\Delta_A d\omega_A'}{2\pi \ 2\pi} e^{-i\Delta_A T} \right.$$
$$\left. \times \varepsilon_s(\omega + \Delta_A) \varepsilon_a(\omega_A' + \Delta_A) \varepsilon_A^*(\omega_A')(F_i + F_{ii} + F_{iii} + F_{iv}) \right]$$
(14)

which can be expressed as

$$S(\omega, T) = P_g |E_p|^2 \int_{-\infty}^{+\infty} \frac{d\Delta_A}{2\pi} S(\omega, T; \Delta_A)$$
(15)

with

$$S(\omega, T; \Delta_A) = (-1)\Im \left[\varepsilon_S^*(\omega) \int_{-\infty}^{+\infty} \frac{d\omega_A'}{2\pi} e^{-i\Delta_A T} \right.$$
$$\left. \varepsilon_s(\omega + \Delta_A) \varepsilon_a(\omega_A' + \Delta_A) \varepsilon_A^*(\omega_A')(F_i + F_{ii} + F_{iii} + F_{iv}) \right]$$
(16)

The Δ_A dispersed signal of eqn (16) is not an observable quantity since it contains more information than the experimental signal $S(\omega,T)$.[26]

3 Signal simulations

We consider a two mode harmonic molecular system, with one low frequency mode ($\tilde{\nu}_l = \omega_l/2\pi c = 50$ cm^{-1}) and one high frequency mode ($\tilde{\nu}_h = 800$ cm^{-1}). Three vibrational states contribute to the sum over states expression (eqn (14)): the high frequency excited state at ω_h, the low frequency excited state at ω_l and a state at $\omega_h + \omega_l$ in which both vibrational modes are excited. Accounting for all possible Liouville pathways, both diagrams (i) and (ii) contribute to a feature at $\omega_P - \omega_h$; the former generates also a side peak shifted to the red of the main feature at $\omega_P - (\omega_h - \omega_l)$ while the latter gives a side peak shifted to the blue at $\omega_P - (\omega_h + \omega_l)$. Similarly, diagrams (iii) and (iv) give rise to a central feature at $\omega_P + \omega_h$ and two side bands. In the present harmonic model the two side bands have the same phase and exhibit a similar behavior, as shown in Fig. 2 where

we display the signal $S(\omega,T)$ for different time delays T. Both the actinic pulse ε_a and the broadband pulse ε_s have a Gaussian envelope with a FWHM of 20 fs and 10 fs, respectively. We emphasize that $S(\omega,T)$, which is proportional to the fifth order polarization $P^{(5)}$, appears as a correction to the stronger $P^{(3)}$ contribution in the total FSRS signal. The actinic-off signal consists of a sharp positive peak centered in $\omega_P - \omega_h$ and a sharp negative peak centered in $\omega_P + \omega_h$ (Fig. S2). When the actinic pulse is switched on, additional features compare at $\omega_P \pm (\omega_h \pm \omega_l)$. As predicted in ref. 19, and quantitatively highlighted in Fig. S3 (ESI†), the inclusion of anharmonicity does not substantially change the above scenario, except for a possible π phase shift between relative side bands associated with the same low frequency mode ω_l. The main as well as the side bands evolve from an absorptive peak to a dispersive shape depending on the delay T. In the side panels of Fig. 2, we show the behavior in time of the number of photons in the red and the blue side of the spectrum, obtained as the integral of $S(\omega,T)$ over the detected frequency ω:

$$N_{red}(T) = \int_{-\infty}^{\omega_P} d\omega S(\omega, T)$$
(17)

$$N_{blue}(T) = \int_{\omega_P}^{\infty} d\omega S(\omega, T)$$
(18)

For each time delay the signal $S(\omega,T)$ is a sum of dispersive and gain/loss absorptive contributions. Only the latter contributes to the integrated signal of eqn (17) and (18), since the dispersive ones cancel out, the gain/loss components of the side bands contribute coherently. Both $N_{red}(T)$ and $N_{blue}(T)$ exhibit damped oscillations in T with the same amplitude and period but the opposite phase. This numerical result can be derived by making some simplifying assumptions. We focus on the response at $\pm(\omega_P - \omega_h)$ generated by diagrams (ii) and (iv). The other contributions can be obtained similarly. For impulsive ε_s and ε_a pulses and a monochromatic ε_p pulse we have

$$N_{red}(T) = - V_\Omega |E_p|^2 |E_s|^2 P_g \Im \left[\int_{-\infty}^{+\infty} \frac{d\omega \, d\Delta_A}{2\pi \ 2\pi} \right.$$
$$\left. \times \frac{e^{-i\Delta_A T}}{[(\omega_P - \omega - \omega_h - i\gamma_h)(-\Delta_A - \omega_l - i\gamma_l)]} \right]$$
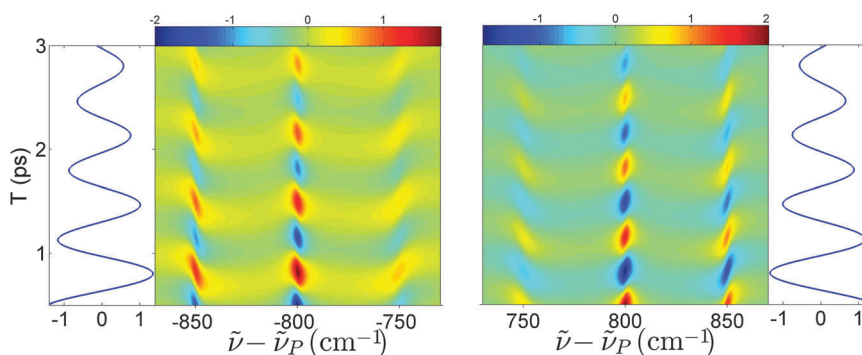(19)

Fig. 2 Two dimensional plot of $S(\omega,T)$, eqn (14), for diagrams (i) and (ii) (on the left) and diagrams (iii) and (iv) (on the right), for a system with one low ($\tilde{\nu}_l = \omega_l/c = 50$ cm^{-1}) and one high frequency mode ($\tilde{\nu}_h = 800$ cm^{-1}); the vibrational dephasing time is $\gamma_l^{-1} = \gamma_h^{-1} = 2.3$ ps. In side panels we show the integrals of the signal over the detected frequency that give the number of photons in the red and in the blue side of the spectrum.

This journal is © the Owner Societies 2015

Phys. Chem. Chem. Phys., 2015, **17**, 10454–10461 | **10457**

for the red side, and

$$N_{blue}(T) = -V_\Omega |E_p|^2 |E_s|^2 P_g \Im \left[\int_{-\infty}^{+\infty} \frac{d\omega \, d\varDelta_A}{2\pi \, 2\pi} \right.$$

$$\left. \times \frac{e^{-i\varDelta_A T}}{[(\omega - \omega_P - \omega_h + i\gamma_h)(\varDelta_A - \omega_l + i\gamma_l)]} \right] \quad (20)$$

for the blue side. V_Ω indicates the quantization volume of the actinic frequencies. Contour integration over $\varDelta_A$ is performed

$$N_{red}(T) \propto -\Im \left[\int_{-\infty}^{+\infty} \frac{d\omega}{2\pi} \frac{i\gamma e^{-i\omega_l T - \gamma_l T}}{(\omega_P - \omega - \omega_h - i\gamma_h)} \right] \quad (21)$$

The denominator in eqn (21) gives a Lorentzian profile

$$\frac{1}{\omega_P - \omega - \omega_h - i\gamma_h} = (\omega_P - \omega - \omega_h + i\gamma_h) L(\omega_P - \omega - \omega_h)$$

which reduces to $i\gamma_h \delta(\omega_P - \omega - \omega_h)$ for small γ_h. This gives

$$N_{red}(T) \propto e^{-\gamma_l T} \sin(\omega_l T) \quad (22)$$

and

$$N_{blue}(T) \propto -e^{-\gamma_l T} \sin(\omega_l T) \quad (23)$$

The total number of photons in the ε_s field is conserved. While the frequency dispersed signal is dominated by the high frequency mode, the information on ω_h is completely lost in the detection of the total field intensity (for example, when performed with a photodiode); the oscillation period $\left(T_N = \frac{2\pi}{\omega_l} \right)$ and the damping factor (γ_l) are determined by the low frequency mode.

Fig. 3 shows the total transmitted energy of the signal, obtained by multiplying the number of photons (18) by $\hbar\omega$, for the red and blue side of the spectrum separately and the total energy oscillation (green line). While the number of photons is conserved in the process, the total pulse energy $I(T) = \int_{-\infty}^{\infty} d\omega S(\omega, T)\omega$ does change.

The role of the actinic pulse is better demonstrated by considering a system with more than one low frequency vibrational mode. In Fig. 4 we use the $\varDelta_A$ dispersed signal (eqn (16)) to study the response of a sample with four low frequency modes (50 cm^{-1}, 80 cm^{-1}, 110 cm^{-1} and 173 cm^{-1}) and one high frequency mode (800 cm^{-1}). For simplicity we consider explicitly levels ω_g, ω_l and ω_h in which only a single mode is excited.

$S(\omega, T = 500 \text{ fs}; \varDelta_A)$ is displayed for various bandwidths of the actinic pump (20 fs, 80 fs and 150 fs of time duration), only the shorter actinic pump pulse is able to excite all the low frequency modes, while the longer pulse can only excite a narrower band of frequencies. The only frequencies of the actinic pulse involved in the process are those involved in the coherence generation with the low frequency mode, belonging to a small region around the resonances. Since the generated coherence is detected at $\omega = \omega_P - (\omega_h - \omega_l)$ (difference between the high and the low frequency mode), reducing the actinic bandwidth truncates the contributions of lower wavenumber frequency far from $\omega = \omega_P - \omega_h$.

Fig. 5 depicts the response of this multi-mode system for an 80 fs actinic pump, showing the time delay dependence of the frequency dispersed spectra and of the frequency integrated signal. The behavior of $N(T)$ is more complex than for a single low frequency mode, since the signal results from the sum of four damped sinusoids, with different amplitudes, depending on the bandwidth of the actinic pump pulse. The contribution from the low modes involved is directly extracted disentangling the four components by the Fourier transform over T of $S(\omega, T)$

$$S(\omega, \Omega) = \int_{-\infty}^{\infty} e^{-i\Omega T} S(\omega, T) \quad (24)$$

which is reproduced in the right panel of Fig. 5. The number of photons $N(T)_{red}$ in the red side and $N(T)_{blue}$ in the blue side
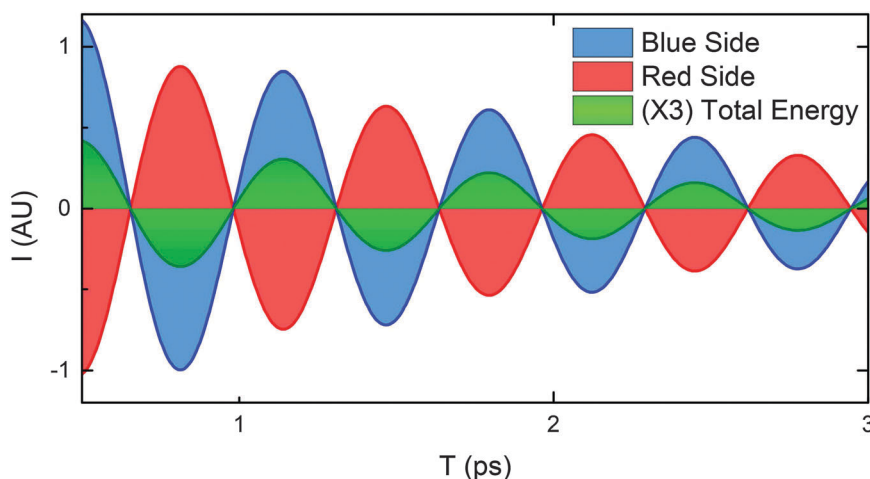

Fig. 3 Total energy balance; the red line indicates the energy oscillation of the signal in the red side of the spectrum, obtained by multiplying the number of photons in Fig. 2 by $\hbar\omega$, while the blue line indicates the energy oscillation in the blue side of the spectrum. The green line shows the total energy oscillation (after a 3-fold expansion). While the total number of photons is conserved in the process, this symmetry is slightly broken if we consider the total energy.
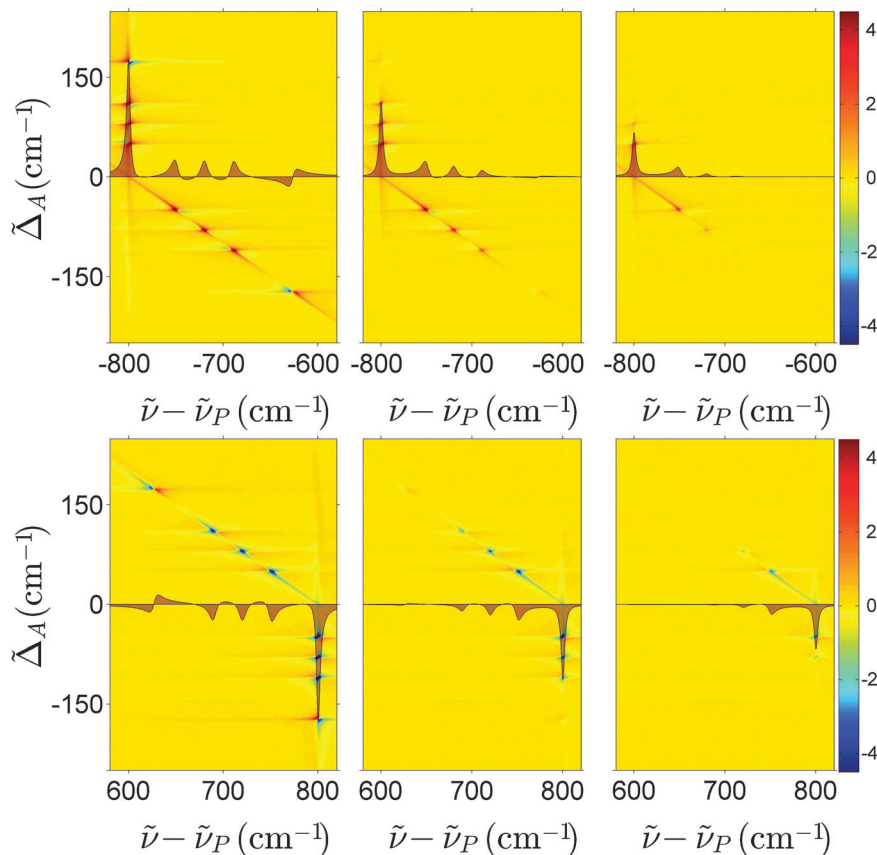
10458 | *Phys. Chem. Chem. Phys.*, 2015, **17**, 10454–10461

This journal is © the Owner Societies 2015

Fig. 4 Δ_A dispersed signal (eqn (16)) and the corresponding integrated signal for diagrams (i) and (ii) (top panel) and (iii) and (iv) (bottom panel) for a system with four low frequency modes (50 cm^{-1}, 80 cm^{-1}, 110 cm^{-1} and 173 cm^{-1}) and one high frequency mode (800 cm^{-1}), calculated at 500 fs of time delay T. The 2D plot of $S(\tilde{\nu}, T = 500$ fs; $\Delta_A)$ is reported by varying the bandwidth of the actinic pump (20 fs, 80 fs and 150 fs of time duration, from the left to the right), showing that a narrower actinic pump pulse is not able to excite all the low frequency modes. The shaded black area reproduces the integral $S(\tilde{\nu}, T = 500$ fs) signal over Δ_A, showing a much more intense contribution at $\tilde{\nu} - \tilde{\nu}_P = \pm\tilde{\nu}_H$.
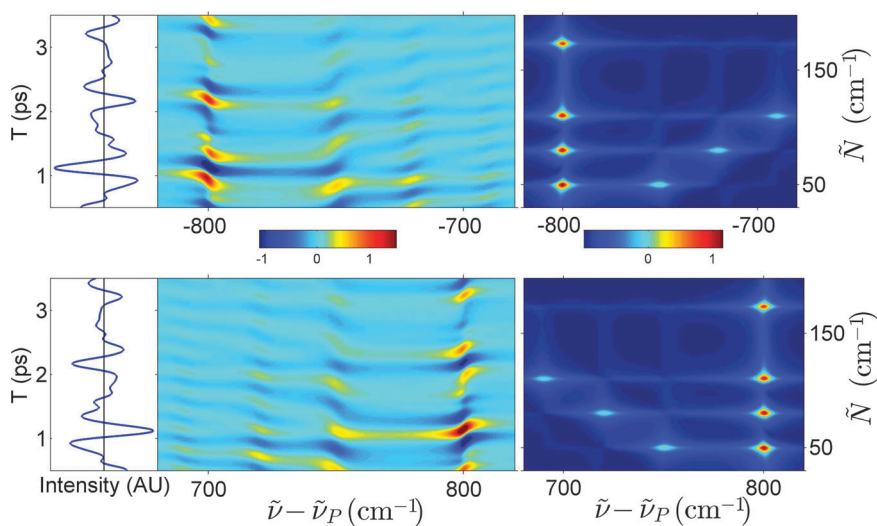

Fig. 5 Central panel: time delay dependent 2D signal $S(\tilde{\nu}, T)$ for diagrams (i) and (ii) (top) and for diagrams (iii) and (iv) (bottom); the response is calculated for a system with four low frequency modes (50 cm^{-1}, 80 cm^{-1}, 110 cm^{-1} and 173 cm^{-1}) and one high frequency mode (800 cm^{-1}) using an 80 fs actinic pump. The number of photons $N_{red/blue}(T)$ is reproduced in the left panel, while in the right one the contributions from all the low frequency modes are disentangled by the Fourier transform $S(\tilde{\nu}/\tilde{N})$.

This journal is © the Owner Societies 2015

Phys. Chem. Chem. Phys., 2015, **17**, 10454–10461 | **10459**

varies with the opposite phase, and the overall number of photons is still conserved.

4 Conclusions

In this paper we have employed a microscopic diagrammatic approach to broadband stimulated Raman spectroscopy with an impulsive off-resonant actinic pump. Expressions for both the red and the blue sides of the spectrum are derived. The coherences created by the impulsive pump cause modifications of the resulting Raman signal as a function of the time delay between the pump and probe pulses, which varies from gain to loss features. The interplay of these features is responsible for a redistribution of photons between the two sides of the spectrum that conserves the total number of photons but leads to an energy flow between fields and matter.

In particular, we have considered three detection modes for fifth-order stimulated Raman measurements that include an actinic initial excitation: the partially integrated red $N_{red}(T)$ or blue $N_{blue}(T)$ (Fig. 2), the frequency integrated 1D signal $I(T)$ (Fig. 3) and the fully dispersed $S(\omega,T)$ (Fig. 2). The first two are 1D and the last is a 2D technique. The integrated signal $I(T)$ probes the total energy exchange between the molecule and the field which reveals Raman resonances. This is also seen by the shift in the blue/red detection. The frequency resolved spectrum carries more information and can show dispersive features which do not contribute to the molecule/field energy exchange.[27] Ideguchi et al.[16,23] had employed the partially integrated detection for a third order measurement of intensity fluctuations and obtained a similar oscillatory behavior to that in our eqn (22) and (23) and Fig. 3.

In a third order experiment the energy flow manifests itself as time domain intensity fluctuations, which can be interpreted as an apparent red and blue shift of the probe pulse.[28] While information on the low frequency vibrational modes of the medium can be retrieved by a Fourier transform, the temporal evolution of the spectrally resolved optical probe is not accessible. The integrated signal directly obtained in ref. 16 can be easily recast from the dispersed signal as we have shown in Fig. 2. In addition, the time resolution brought about by the fifth order process enables the collection of snapshots of the energy transfer pathway, while the frequency dispersed detection allows dissecting the time dependence of the contribution corresponding to a single spectral component. Although this does not provide additional information from the material perspective, it reveals the mechanism underlying the energy redistribution pathway. Specifically, as seen in Fig. 2 the low frequency coherence does not generate a spectral shift but rather a modulation of the first momentum of the broadband probe spectrum.

Acknowledgements

References

1   M. Yoshizawa, Y. Hattori and T. Kobayashi, *Phys. Rev. B: Condens. Matter Mater. Phys.*, 1994, **49**, 13259–13262.

2   D. W. McCamant, P. Kukura, S. Yoon and R. A. Mathies, *Rev. Sci. Instrum.*, 2004, **75**, 4971.

3   P. Kukura, D. W. McCamant, S. Yoon, D. B. Wandschneider and R. A. Mathies, *Science*, 2005, **310**, 1006–1009.

4   S. Laimgruber, H. Schachenmayr, B. Schmidt, W. Zinth and P. Gilch, *Appl. Phys. B: Lasers Opt.*, 2006, **85**, 557–564.

5   C. Fang, R. R. Frontiera, R. Tran and R. A. Mathies, *Nature*, 2009, **462**, 200–204.

6   S. A. Kovalenko, A. L. Dobryakov and N. P. Ernsting, *Rev. Sci. Instrum.*, 2011, **82**, 063102.

7   A. L. Dobryakov, I. Ioffe, A. A. Granovsky, N. P. Ernsting and S. A. Kovalenko, *J. Chem. Phys.*, 2012, **137**, 244505.

8   E. Pontecorvo, S. Kapetanaki, M. Badioli, D. Brida, M. Marangoni, G. Cerullo and T. Scopigno, *Opt. Express*, 2011, **19**, 1107.

9   E. Pontecorvo, C. Ferrante, C. G. Elles and T. Scopigno, *Opt. Express*, 2013, **21**, 6866–6872.

10 E. Pontecorvo, C. Ferrante, C. G. Elles and T. Scopigno, *J. Phys. Chem. B*, 2014, **118**, 6915–6921.

11 H. Kuramochi, S. Takeuchi and T. Tahara, *J. Phys. Chem. Lett.*, 2012, **3**, 2025–2029.

12 F. Provencher, N. Bérubé, A. W. Parker, G. M. Greetham, M. Towrie, C. Hellmann, M. Côté, N. Stingelin, C. Silva and S. C. Hayes, *Nat. Commun.*, 2014, **5**, 4288.

13 M. Kloz, R. van Grondelle and J. T. Kennis, *Phys. Chem. Chem. Phys.*, 2011, **13**, 18123.

14 B. Mallick, A. Lakhsmanna and S. Umapathy, *J. Raman Spectrosc.*, 2011, **42**, 1883–1890.

15 U. Harbola, S. Umapathy and S. Mukamel, *Phys. Rev. A: At., Mol., Opt. Phys.*, 2013, **88**, 011801.

16 T. Ideguchi, S. Holzner, M. Yan, G. Guelachvili, T. W. Hänsch and N. Picqué, 2014, arXiv:1403.3814.

17 P. Kukura, R. Frontiera and R. A. Mathies, *Phys. Rev. Lett.*, 2006, **96**, 238303.

18 R. D. Mehlenbacher, B. Lyons, K. C. Wilson, Y. Du and D. W. McCamant, *J. Chem. Phys.*, 2009, **131**, 244512.

19 Z. Sun, B. Fu, D. H. Zhang and S.-Y. Lee, *J. Chem. Phys.*, 2009, **130**, 044312.

20 B. Dunlap, K. C. Wilson and D. W. McCamant, *J. Phys. Chem. A*, 2013, **117**, 6205–6216.

21 K. J. Kubarych, C. J. Milne and R. J. D. Miller, *Int. Rev. Phys. Chem.*, 2003, **22**, 497–532.

22 C. J. Milne, Y. L. Li, T. L. C. Jansen, L. Huang and R. J. D. Miller, *J. Phys. Chem. B*, 2006, **110**, 19867–19876.

23 T. Ideguchi, S. Holzner, B. Bernhardt, G. Guelachvili, N. Picqué and T. W. Hänsch, *Nature*, 2013, **502**, 355–358.

24 K. E. Dorfman, B. P. Fingerhut and S. Mukamel, *J. Chem. Phys.*, 2013, **139**, 124113.

25 S. Rahav and S. Mukamel, *Advances in Atomic, Molecular, and Optical Physics*, 2010, vol. 59.

26 B. P. Fingerhut, K. E. Dorfman and S. Mukamel, *J. Chem. Theory Comput.*, 2014, **10**, 1172–1188.

27 S. Rahav and S. Mukamel, *Proc. Natl. Acad. Sci. U. S. A.*, 2010, **107**, 4825–4829.

28 Y. Silberberg, *Nature*, 2013, **502**, 307–308.

This journal is © the Owner Societies 2015

Phys. Chem. Chem. Phys., 2015, **17**, 10454–10461 | **10461**